

Unique Combinations of Differently Shaped Equatorial Plasma Bubbles Occurring Within a Small Longitude Range

Deepak Kumar Karan¹, Richard W. Eastes¹, Carlos R. Martinis², Robert E. Daniell³,
Stanley C. Solomon⁴ and William E. McClintock¹

¹Laboratory for Atmospheric and Space Physics, University of Colorado, Boulder, CO, USA

²Center for Space Physics, Boston University, MA, USA

³Ionospheric Physics, Stoughton, MA, USA

⁴High Altitude Observatory, National Center for Atmospheric Research, Boulder, CO, USA

Corresponding author: Deepak Kumar Karan (Deepak.Karan@lasp.colorado.edu)

Key Points:

- Differently shaped EPBs are observed simultaneously within a small longitude of $\sim 10^\circ$
- Observations indicate longitudinal variations in EPBs' zonal drift velocities at the magnetic equator and EIA crests
- Indication of the effect of small spatial scale E-region density, electric field, neutral wind variations, or a combination of them

Key Words: NASA GOLD mission, Equatorial Plasma Bubbles, EPB Morphology, Plasma Irregularities, Nighttime ionosphere, OI 135.6 nm nightglow

Abstract:

On 12 October 2020 and 26 December 2021, NASA's Global-scale Observations of the Limb and Disk (GOLD) mission observed differently shaped EPBs simultaneously within $\sim 10^\circ$ longitude, near the subsatellite point and over the Atlantic, respectively which is unusual. On 12 October 2020, three EPBs with differing curvatures were observed in a $\sim 12^\circ$ longitude sector. The westside EPB was curved towards the east, in a C-shape. The middle was straight. The eastside EPB was curved westward, in a reversed C-shape. In the second case, 26 December 2021, in a smaller longitude range of $\sim 6^\circ$ adjacent C-shaped and reversed C-shaped EPBs were observed. EPBs'

zonal drift velocities at the magnetic equator and both EIA crests were compared. These occurrences of oppositely shaped EPBs simultaneously in a narrow longitude may indicate that small-scale longitudinal variations in the E-region density, electric field, neutral wind variations, or a combination of them were present.

Plain Language Summary:

The post-sunset ionosphere becomes conducive to the formation of plasma irregularities associated with depleted plasma densities. In the images obtained from space or ground, these plasma depleted regions appear as latitudinally elongated dark bands, which are known as “equatorial plasma bubbles (EPBs)”. Satellite communication and navigation systems are adversely affected when the trans-ionospheric radio signals travel through the EPBs. Thus, investigations of EPBs’ formation and development are important. In 2-D airglow images, the EPBs appear to be straight (aligned along the magnetic field lines). However, sometimes the poleward extensions of the EPBs can be tilted eastward or westward from the magnetic field line resembling either a C-shape or reversed C-shape, respectively. These differently shaped EPBs have been observed before. But, NASA’s Global-scale Observations of the Limb and Disk (GOLD) mission observed them simultaneously within $\sim 12^\circ$ and 6° longitudes on 12 October 2020 and 26 December 2021 which is unusual. Such occurrence of opposite-shaped EPBs within a small longitude range indicates small-scale longitudinal variations in the E-region density, neutral winds, electric fields, or a combination of them. We present detailed observations of these two unique events with possible explanations.

Introduction:

Equatorial plasma bubbles (EPBs) are manifestations of post-sunset plasma irregularities associated with depleted plasma densities that occur over the equatorial and low-latitude ionosphere. Trans-ionospheric radio wave propagation for communication, navigation, and timing is adversely affected when passing through these plasma irregularities. Thus, the investigation of plasma irregularities is an important priority for researchers, with societal implications. The formation and development of plasma irregularities depend on several factors such as vertical and horizontal ionospheric density gradient (both neutral and plasma), background neutral winds, zonal electric fields, chemical recombination, and atmospheric waves (Sultan, 1996; Taori et al., 2011;

Liu et al., 2017; Bhattacharyya, 2022). EPBs are expected to be aligned to the magnetic field lines, and when they are, they are straight in rectified airglow images. However, in some cases, the poleward extensions of the EPBs are tilted eastward or westward from the magnetic field line resembling a C-shape or reversed C-shape, respectively.

Using a ground-based all-sky airglow imaging system, the westward tilt of the airglow depletions to the magnetic field lines was reported (Mendillo and Baumgardner, 1982; Mendillo and Tyler, 1983). A decrease of the eastward plasma drift velocity with increasing altitude (latitude) could be produced if the eastward neutral wind velocity also decreases with altitude (latitude) (Rishbeth, 1972; Anderson and Mendillo, 1983). This could form reversed C-shape EPB. Such a decrease in zonal neutral wind speed at the EIA crests due to larger ion drag has been observed by Dynamics Explorer-2 (DE-2) satellite (Raghavarao et al., 1991) and ground-based Fabry-Perot interferometer (Martinis et al., 2001, 2003). Reversed C-shape EPBs were observed in the OI 135.6-nm emission images by the Global Ultraviolet Imager (GUVI) on board the Thermosphere, Ionosphere, Mesosphere Energetics and Dynamics (TIMED) satellite (Kelley et al., 2003). Kil et al. (2009) explained the reversed C-shape structure by (a) the reduction of the eastward plasma flow inside the EPB due to the development of a polarization electric field that retarded at higher apex height (indicated by Woodman and La Hoz, 1976) and (b) the latitudinal variation of the eastward drift of the background ionosphere, as explained by Anderson and Mendillo (1983) and Martinis et al. (2003). Huba et al. (2009) have investigated the model (HWM93) zonal winds' effect on the EPBs' morphology through SAMI3, a three-dimensional modeling simulation. They found that stronger neutral zonal winds at lower altitudes and a decrease of velocity at latitudes away from the equator cause the reversed C-shape EPBs which agreed with the observations reported by Kelley et al. (2003) and Kil et al. (2009).

C-shape EPBs were reported for the first time using the Jicamarca radar backscatter maps (Woodman and La Hoz, 1976); where no explanation for the formation mechanism was given. During the early night, zonal plasma drifts over the off-equatorial latitudes were observed to be stronger than the equatorial latitudes using electric field measurements from DE-2 (Aggson et al., 1987) and ground-based airglow measurements (Martinis et al., 2003). These latitudinal variations in the zonal plasma drifts can be related to their altitudinal variations at the magnetic equator. Even if the zonal neutral wind is constant with altitude, plasma drifts can vary with altitude due to the variations in the Pedersen conductivity. Zalesak et al. (1982) incorporated an eastward neutral

wind in the equatorial F region and E region Pedersen conductivity effects in their two-dimensional numerical simulation and found that the rising EPBs were caught up in the vertical shears of the plasma motion, resulting in the ‘C’ shape. Thus, the actual EPB shape depends strongly on both the zonal neutral wind profile and the Pedersen conductivity. SAMI3 produced a C-shape EPB when HWM07 neutral wind was taken as input (Huba et al., 2009). In this case, the HWM07 zonal winds produced a strong westward drift at low altitudes which caused an eastward tilt of EPB (C-shape EPB) at higher altitudes. Further, maximum eastward zonal neutral winds over low latitudes could favor the C-shape EPB.

On October 12, 2020, the NASA Global-scale Observations of the Limb and Disk (GOLD) mission observed three consecutive EPBs; a C-shape, a straight, and a reversed C-shape EPBs, within $\sim 12^\circ$ longitudes at magnetic equatorial latitudes. The observed longitude is close to the GOLD’s subsatellite point ($\sim 47^\circ$ W). In another case on 26 December 2021, a reversed C-shape and C-shape EPB were observed sidewise within $\sim 6^\circ$ longitude. While there are numerous images with EPBs having different shapes, these two examples of consecutive EPBs with reversing shapes within a small longitude range are unusual. This points to small longitudinal variations in the E-region density, electric field, neutral wind variations, or a combination of them. We report detailed observations of these two unique and rare events and discuss their possible formation mechanisms.

Data:

Nighttime OI 135.6 nm partial disk scans made by the GOLD imager are the data used in this study. The GOLD imager was launched on a commercial communications satellite on 25 January 2018 and it is in geostationary orbit at 47.5° W. Nominal operations and observations started on 9 October 2018. It has two identical spectrographs that obtain the Earth images in the far-ultraviolet (FUV) range, at ~ 134 - 162 nm wavelength. It measures the column-integrated emission rate along the line of sight. When geolocating the observations, an emission altitude of 300 km is assumed. GOLD can observe the American, Atlantic, and Western African longitudes, which provides a unique opportunity to unambiguously observe the spatial-temporal evolution of various ionospheric-thermospheric features in this active region of the Equatorial Ionization Anomaly (EIA). The nighttime L1C disk images are obtained at a cadence of 15 minutes and binned to 90×80 km at the nadir. Detailed information about the GOLD instrument and observation modes are discussed in Eastes et al., (2017, 2020) and McClintock et al., (2020, 2023).

Results and Discussion:

GOLD takes nighttime disk observations using both channels A and B (CHA and CHB hereafter). Most individual scans cover $\sim 45^\circ$ in longitude, ~ 3 hours in local time, just to the east of the sunset terminator. Starting from 20:10 UT, CHB takes nighttime partial disk images, alternating between the Northern and Southern hemispheres until 23:10 UT. From 23:10 to 00:09 UT (the next day) simultaneous observations of the Northern and Southern hemispheres are made using CHA and CHB. The observation sequence is described in detail by Karan, et al. (2020).

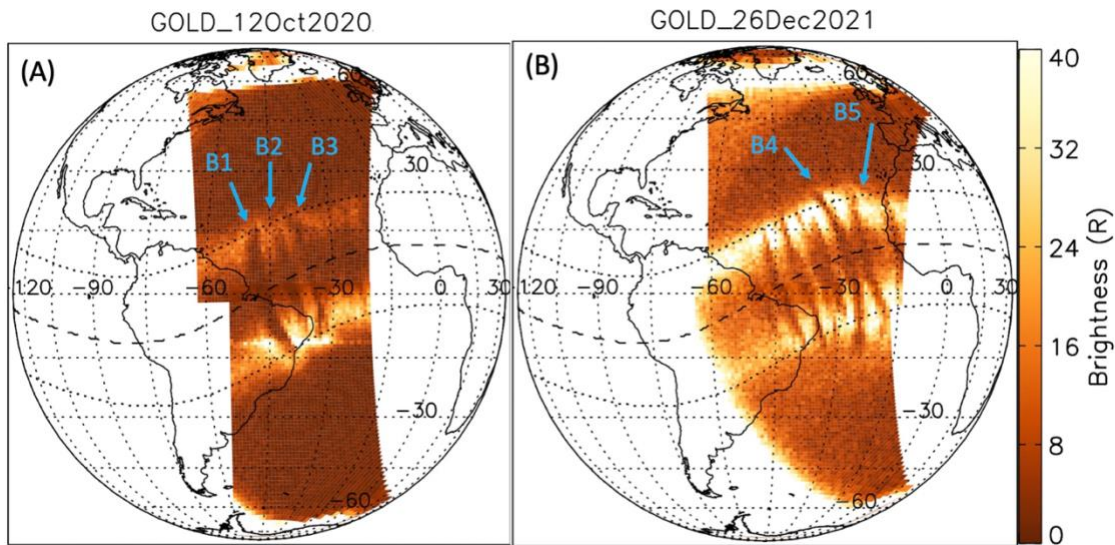


Figure 1. (A) The nighttime images obtained by GOLD in OI 135.6 nm simultaneously by CHA and CHB at 23:10 UT on 12 October 2020 are combined. The white dashed line shows the geomagnetic equator. The two bright emission patches seen at all longitudes on either side of the magnetic equator are the EIA crests. EPBs are the depletions in brightness across the EIA crests. The C-shape, straight, and reversed C-shape EPBs are marked as B1, B2, and B3, respectively. (B) Similar to Figure A but the CHB images obtained on 26 December 2021 at 22:40 UT and 22:55 UT are combined. The reversed C-shape and C-shape EPBs are marked as B4 and B5.

Figure 1A shows simultaneous images obtained by CHA and CHB from the northern and southern hemispheres, respectively on 12 October 2020 at 23:10 UT. The white dashed line marks the geomagnetic equator. The emissions peaking on either side of the geomagnetic equator are the EIA crests. At 10°S GLat there is a faint data artifact. At that latitude, there appears to be a longitudinally extended region of slightly brighter emission, but EPBs are still apparent as depletions in the brightness across the EIA crests. This artifact is due to the high voltage being too low during the flat field measurements, which is explained in Section 3.1.18 of the GOLD data release note Rev 4.6 (<https://gold.cs.ucf.edu/wp->

141 content/documentation/GOLD_Release_Notes_Rev4.6.pdf). Over the Eastern side of South
142 America ($\sim 50^\circ$ - 35° W longitudes) there are three distinct and differently shaped EPBs. This
143 longitude range is close to the crossing of the geographic and geomagnetic equators and near the
144 subsatellite location. The EPB on the left side (marked as B1) has a C-shape, the one in the middle
145 (B2) is straight, whereas the right EPB (B3) has a reversed C-shape. B3 appears to be bifurcated
146 at the south (S) EIA crests. Each of these EPB shapes has been observed previously by others and
147 by GOLD, but in the observations on October 12, 2020, the three distinct EPB shapes occurred
148 consecutively over a narrow longitude range ($\sim 12^\circ$). Contrary to this case, the C- and reversed C-
149 shape EPBs were observed in an opposite order within $\sim 30^\circ$ and 20° W longitudes on 26 December
150 2021. Consecutive images taken by CHB at 22:40 UT and 22:55 UT on 26 December 2021 are
151 combined and shown in Figure 1B. The EPBs at the west side of 30° W longitude appear to be
152 straight. But the EPBs (B4 and B5) observed within $\sim 30^\circ$ and 20° W longitudes are of opposite
153 shapes and are the focus in this image. The reversed C-shape EPB (B4) is observed to the west of
154 the C-shape EPB (B5) and the two are separated by $\sim 6^\circ$ at their magnetic equators (Figure 1B). In
155 both cases (Figure 1A, B) the EPBs are observed multiple times between $\sim 19:30$ to 22.00 LT
156 (Local Time) with initial observations around ~ 2 hrs after the local sunset. To investigate the
157 different EPBs' shapes (B1 to B5) observed at similar local times but within a small longitude

range, we derived their zonal drift velocities at the magnetic equator and EIA crest latitudes. The EPB drift velocity derivation method is explained below for 12 October 2020 and is also used for 26 December 2021.

For the investigation, images are first transferred into magnetic coordinates (Laundal and Richmond, 2017; Thébault et al., 2015). Figures 2 (A), (B), (C), and (D) show the images at 23:10, 23:25, 23:40, and 23:55 UT on 12 October 2020, respectively. At 23:10 UT (Figure 2A) the locations of B1, B2, and B3 at the magnetic equator are ($\sim 47^\circ$ W Glon, 0.5° N Glat, 26.5° Mlon), ($\sim 40^\circ$ W Glon, 2.5° N Glat, 33.2° Mlon), and ($\sim 35.5^\circ$ W Glon, 5.7° N Glat, 38.5° Mlon), respectively. Next, we obtain the EPBs' longitudes at three different magnetic latitude ranges; (10° to 15°), (-6° to 6°), and (-15° to -10°), shown by green, blue, and magenta boxes, respectively, in Figure 2. These latitude ranges distinguish the EIA crests from the magnetic equatorial region. Since B2 reaches lower latitudes than B1 and B3, the EIA crest latitude ranges for B2 are considered to be (6° to 12°) and (-12° to -6°). The brightness along the latitudes in each box is summed at each longitude. From the longitudinal variations of the summed brightness, the EPBs' longitudes in an image were obtained. This method is explained in detail by Karan et al., 2020. B1, B2, and B3 longitudes are obtained from all the nighttime partial disk images on October 12,

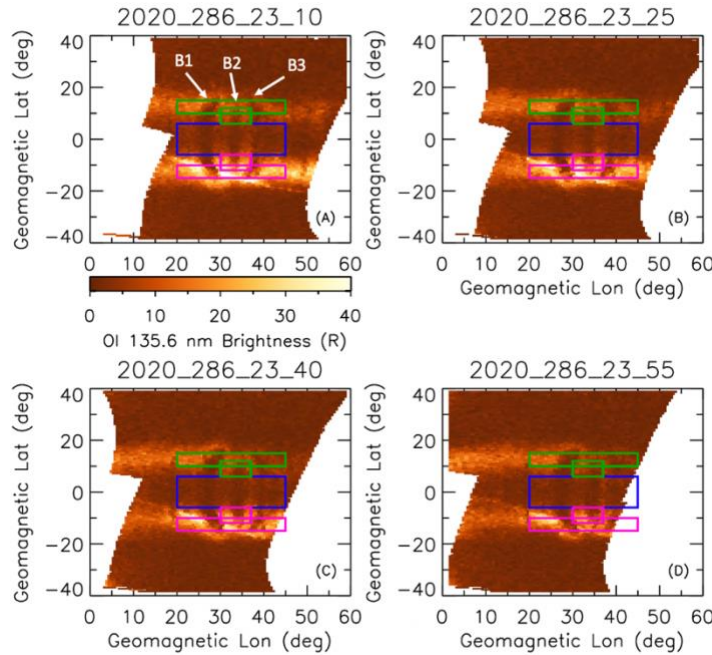


Figure 2. (A, B, C, and D) show the nighttime images observed by GOLD at 23:10, 23:25, 23:40, and 23:55 UT on 12 October 2020, respectively in geomagnetic coordinates. The green, blue, and magenta boxes mark the N- crest, magnetic equator, and S- crest of EIA latitudes (common on each panel).

2020, which are shown in Figure 3A. Following the same method, B4 and B5 longitudes on 26 December 2021 are obtained and are shown in Figure 3B.

EPB longitudes obtained at the magnetic equator, N and S EIA crests latitudes are shown by blue dots, green plus, and red cross symbols, respectively in Figure 3. One of the advantages of the GOLD observations is that EPB locations are obtained multiple times. Earlier detection of B3 at 22:10 UT is due to the GOLD imager's observation sequence from east to west following the sunset terminator. EPBs are developed at the geomagnetic equator and grow to higher altitudes and latitudes. Thus, EPBs are detected first closer to equatorial latitudes. All EPBs shift eastward with time at each latitude range. From the changes in the longitudes, EPB drift velocities are derived at the three latitude ranges and are listed in the table-1.

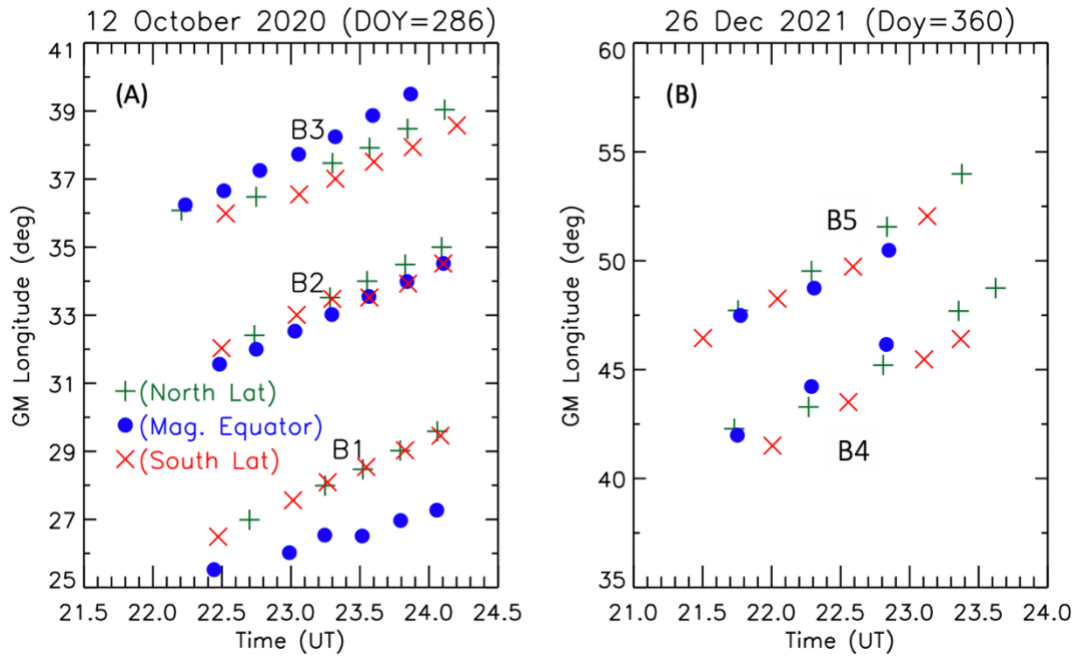


Figure 3 shows EPB longitudes at different times of observations on (A) 12 October 2020 and (B) 26 December 2021. Blue dot, green plus, and red cross symbols indicate to longitudes as obtained at the magnetic equator, N and S EIA crests latitudes, respectively.

Table 1. EPBs' zonal drift velocities (m/s) at the magnetic equator, N and S EIA crest latitudes on 12 October 2020 and 26 December 2021. Positive drift velocities are eastward.

	12 October 2020			26 December 2021	
Magnetic Latitude Zone	B1	B2	B3	B4	B5
N-EIA crest	65 ± 2	62 ± 4	57 ± 9	115 ± 20	123 ± 16
Equator	48 ± 6	62 ± 2	68 ± 4	125 ± 7	88 ± 14
S-EIA crest	62 ± 3	61 ± 5	52 ± 5	108 ± 3	104 ± 14

From the EPB zonal drift velocities, it can be seen that for B1 and B5, the zonal drift velocities at the EIA crests are higher than at the magnetic equator which is consistent with their C-shape. Bubbles B3 and B4 show opposite behavior and higher drift velocities at the magnetic equator. On 12 October 2020, the drift velocities at both EIA crest latitudes decreased from west to east (B1 to B3), whereas increased at the magnetic equatorial latitudes. So, we calculated the inter-bubble separations at different observation times to better understand the connection between the drift velocities and EPBs shapes. Due to the lower zonal velocity of B1 (C-shape) at the magnetic equator and its location, west of B3, the separation of B1 from B3 increased from $\sim 11.1^\circ$ to 12.8° during ~ 22.5 - 24.0 UT. On the other hand, B5 (C-shape) is east of B4. So, the separation between B4 and B5 decreased from $\sim 5.5^\circ$ to $\sim 4.3^\circ$ during ~ 21.8 - 22.8 UT. Therefore, if an EPB with higher zonal drift velocity at the magnetic equator is located near a C-shape EPB (moving slower at the equator), then it separates more or gets closer to the C-shape EPB depending on its location (whether to the east or west of the C-shape EPB).

At the EIA crests, where the electron densities are largest, we would expect larger ion drag forces and lower zonal wind speeds than at the magnetic equator. As a result, EPB zonal drift velocity would be lowered at these EIA crests than at the equator (Raghavarao et al., 1991; Martinis et al., 2001, 2003; Valladares et al., 2002) producing a reversed C-shape EPB (Huba et al., 2009). This is the case with B3 and B4. Since B2 did not reach the peak of the EIA crests, ion drag effects might not be too different at the three latitude ranges and hence, no latitudinal variation in the shape of B2 is observed. The ion drag force mechanism does not explain the formation of the C-

shape EPBs (B1 and B5), where the drift velocities at the EIA crests are higher than at the equator. A possible mechanism for this could be due to the contribution of plasma flux tube integrated neutral zonal wind and F region Pedersen conductivity (Aggson et al., 1987; Martinis et al., 2003; Huba et al., 2009). A strong westward zonal wind in the lower F region producing an eastward tilt at higher altitudes as reported by Huba et al., (2009) is another possibility for the C-shape EPBs like B1 and B5. This is particularly important during post-sunset conditions when any potential contribution from E-region could be important. Martinis et al. (2003) compared zonal drifts measured near the magnetic equator and away from it. The results showed that early in the night (~20:00 to 22:30 LT) when E-region contribution can be important, drifts near the equator were slower than later when no significant E-region contribution exists. In the present case, the GOLD imager scanned the C-shape B1 apex at about 23:15 UT (~20:00 LT) which was about 2 hrs past the E-layer sunset. The C-shape EPB (B5) on 26 December 2021 was scanned at about 22:53 UT (~21:15 LT) which was 2.5 hrs past the E-layer sunset. So, during these early nights the slower zonal plasma drifts at the equatorial latitudes as suggested by Martinis et al., (2003) could have caused the C-shape of B1 and B5.

While the above-mentioned observations and mechanisms may explain the C and reversed C-shape EPBs, the occurrence of both shape EPBs within a small ($\sim 12^\circ$ and $\sim 6^\circ$) longitude range is significant here. This indicates the existence of small spatial scale E-region density, electric field, neutral wind variations, or a combination of them affecting the EPB shapes. Lower atmospheric gravity waves or in-situ generated secondary gravity waves can cause small-scale longitudinal variations in the E-region density (Mandal et al., 2019; Manju et al., 2023; Pallamraju et al., 2016; Yoshimura et al., 2003). The other potential factor is the longitudinal variation of the electric field. Before about 22 LT, the presence of a perturbation electric field associated with the R-T instability contributes to the vertical as well as zonal movement of an EPB (Huba and Joyce, 2010). The upward movement of an EPB causes an increase in its latitudinal extent, as it maps along geomagnetic field lines which can be seen for B1 and B2. The shorter latitudinal extent of B2 indicates that the EPB did not rise to the heights above the dip equator as reached by B1 and B3. This could be due to the prevalent ambient ionospheric-thermospheric conditions at the longitude where B2 was generated. Small spatial scale variations ($\sim 3^\circ$ longitude) in the daytime equatorial electric fields have been reported (Karan and Pallamraju (2017). B1 and B3 are separated by $\sim 11.5^\circ$ longitudes at 23:10 UT. Between the ~ 46 minutes LT, the ambient zonal and

vertical plasma drifts also change considerably (Fejer, 2011) which could affect the different EPBs shapes. But, B4 and B5 are separated by $\sim 5.5^\circ$ longitudes (which is ~ 22 minutes). So, the difference in the ambient zonal and vertical plasma drifts may not be significant. Contributions from the longitudinal variations of the zonal neutral winds cannot be ruled out. We observed that over the magnetic equatorial latitudes, the zonal plasma drifts are slower at the longitudes of B1 and B5 as compared to the longitudes of other EPBs (see Table-1). Further, the zonal plasma drifts depend on both E and F region conductivities and neutral zonal wind shears; both vary in altitude and latitude. The post-sunset prereversal enhancement (PRE) strength (Haerendel et al., 1992) changes the shear altitude which affects the EPBs shape. So, longitudinal variations in PRE-strength could also have contributed to forming the observed EPB shapes. Overall the dynamics of the EPBs are quite complex, particularly in the initial phase after their development. So, the different shapes at such a small longitude range could be due to the combined effect of the factors mentioned above.

On 12 October 2020, the EPBs were observed close to the South Atlantic Anomaly (SAA) regions. Because of particle radiation in the SAA, uncertainties in the ICON (Ionospheric Connection Explorer) measurements are too large for them to be useful. On 26 December 2021, ICON concurrent measurements were not available in the same spatial area of B4 and B5. One potential effect that may be excluded is geomagnetic activity, since in both cases, the geomagnetic conditions were quiet. Unfortunately, it is not possible to conclusively identify the mechanisms responsible for the occurrence of different EPB shapes within a small longitude range. However, observations reported in this study provide a challenge for numerical simulations and an opportunity for advancing our understanding of the I-T system. Numerical simulation efforts are required to understand such events. Considering the adverse impact of ionospheric plasma irregularities on trans-ionospheric satellite communication and navigation, the present observation needs immediate attention in the space science research community for further investigations.

Conclusions:

The C-shape and reversed C-shape EPBs have been observed previously. However, in this paper, we report two cases when NASA's GOLD imager observed these differently shaped EPBs within $\sim 10^\circ$ longitudes which have not been reported before. Three consecutive EPBs with C-shape, straight, and reversed C-shape were observed within the $\sim 12^\circ$ longitude range over the eastern side

of South America on October 12, 2020. In another case on 26 December 2021, a reversed C-shape and C-shape EPB were observed within the $\sim 6^\circ$ longitudes over the Atlantic sector. These are observed close to the crossing of geographic and geomagnetic equators and, close to the subsatellite point of the GOLD imager. The calculated EPB drift velocities at the magnetic equator and EIA crest latitudes are different which could be due to the latitudinal variations of the zonal wind speeds that drive their motions. Also, the inter-bubble separations corroborated these findings. Further, different EPBs' shapes in such small longitude ranges indicate small-scale longitudinal differences in the E-region density, electric field, neutral wind variations, or a combination of them. These rare and unique observations are crucial for a better understanding of plasma irregularities and provide a challenge for numerical simulations to advance our understanding of the I-T system.

Acknowledgements:

This research is supported by NASA contract 80GSFC18C0061 to the University of Colorado.

Open Research:

The GOLD L1C nighttime partial disk data presented in this paper (Level 1C – NI1) can be accessed at the GOLD Science Data Center (<http://gold.cs.ucf.edu/search/>). Please be sure to read the GOLD data release note Rev 4.6 (https://gold.cs.ucf.edu/wp-content/documentation/GOLD_Release_Notes_Rev4.6.pdf).

Reference:

Aggson, T. L., Maynard, N. C., Herrero, F. A., Mayr, H. G., Brace, L. H., and Liebrecht, M. C. (1987), Geomagnetic equatorial anomaly in zonal plasma flow, *J. Geophys. Res.*, 92(A1), 311–315, doi:10.1029/JA092iA01p00311.

Anderson, D.N. and Mendillo, M. (1983), Ionospheric conditions affecting the evolution of equatorial plasma depletions. *Geophys. Res. Lett.*, 10: 541-544.
<https://doi.org/10.1029/GL010i007p00541>

Bhattacharyya, A. (2022). Equatorial Plasma Bubbles: A Review. *Atmosphere* 2022, 13, 1637.
<https://doi.org/10.3390/atmos13101637>

Eastes, R. W., McClintock, W. E., Burns, A. G., Anderson, D. N., Andersson, L., Codrescu, M.,
 et al. (2017). The Global-scale Observations of the Limb and Disk (GOLD) mission. *Space Sci*
Rev, 212, 383, doi:10.1007/s11214-017-0392-2

Eastes, R. W., McClintock, W. E., Burns, A. G., Anderson, D. N., Andersson, L., Aryal, S., et al.
 (2020). Initial observations by the GOLD mission. *J. Geophys. Res. Space Physics*, 125,
 e2020JA027823, doi:10.1029/2020JA027823

Eastes, R. W., Karan, D. K., Martinis, C., Daniell, R. E., Gan, Q., Burns, A. G., & McClintock,
 W. E. (2023). GOLD observations of longitudinal variations in the nighttime equatorial
 ionization anomaly (EIA) crests' latitudes. *Journal of Geophysical Research: Space Physics*, 128,
 e2022JA031007. <https://doi.org/10.1029/2022JA031007>

Fejer, B.G. Low Latitude Ionospheric Electrodynamics. *Space Sci Rev* 158, 145–166 (2011).
<https://doi.org/10.1007/s11214-010-9690-7>

Haerendel, G., J. V. Eccles, and S. C. akir, Theory for modeling the equatorial evening
 ionosphere and the origin of the shear in the horizontal plasma flow, *J. Geophys. Res.*, 97, 1209–
 1223, 1992.

Huba, J. D., S. L. Ossakow, G. Joyce, J. Krall, and S. L. England (2009), Three-dimensional
 equatorial spread F modeling: Zonal neutral wind effects, *Geophys. Res. Lett.*, 36, L19106,
 doi:10.1029/2009GL040284.

Huba, J. D., and G. Joyce (2010), Global modeling of equatorial plasma bubbles, *Geophys. Res.*
Lett., 37, L17104, doi:10.1029/2010GL044281.

335 Karan, D. K., and D. Pallamraju, (2017). Small-scale longitudinal variations in the daytime
 336 equatorial thermospheric wave dynamics as inferred from oxygen dayglow emissions. *J.*
 337 *Geophys. Res. Space Physics*, 122, 6528-6542, doi:10.1002/2017JA023891
 338
 339 Karan, D. K., Daniell, R. E., England, S. L., Martinis, C. R., Eastes, R. W., Burns, A. G., &
 340 McClintock, W. E. (2020). First zonal drift velocity measurement of equatorial plasma bubbles
 341 (EPBs) from a geostationary orbit using GOLD data. *J. Geophys. Res. Space Physics*, 125,
 342 e2020JA028173, doi:10.1029/2020JA028173
 343
 344 Kelley, M. C., Makela, J. J., Paxton, L. J., Kamalabadi, F., Comberiate, J. M., and Kil, H. (2003),
 345 The first coordinated ground- and space-based optical observations of equatorial plasma bubbles,
 346 *Geophys. Res. Lett.*, 30, 1766, doi:10.1029/2003GL017301, 14.
 347
 348 Kil, H., R. A. Heelis, L. J. Paxton, and S.-J. Oh (2009), Formation of a plasma depletion shell in
 349 the equatorial ionosphere, *J. Geophys. Res.*, 114, A11302, doi:10.1029/2009JA014369.
 350
 351 Laundal, K. M., and Richmond, A. D. (2017) Magnetic Coordinate Systems, *Space Sci Rev*, 206,
 352 27-59. <https://doi.org/10.1007/s11214-016-0275-y>
 353
 354 Liu, H., N. Pedatella, and K. Hocke (2017), Medium-scale gravity wave activity in the
 355 bottomside F region in tropical regions, *Geophys. Res. Lett.*, 44, 7099–7105,
 356 doi:10.1002/2017GL073855.
 357
 358 Mandal, S., Pallamraju, D., Karan, D. K., Phadke, K. A., Singh, R. P., & Suryawanshi, P. (2019).
 359 On deriving gravity wave characteristics in the daytime upper atmosphere using radio technique.
 360 *Journal of Geophysical Research: Space Physics*, 124, 6985– 6997.
 361 <https://doi.org/10.1029/2019JA026723>
 362
 363 Manju, G., Mridula, N., Sruthi, T. V., Pant, T. K., Aswathy, R. P., Sreelatha, P., et al. (2023).
 364 Generation of post sunset E region electron density stratifications at the magnetic equator: An

analysis using in situ measurements and theoretical estimations. *Journal of Geophysical Research: Space Physics*, 128, e2022JA030903. <https://doi.org/10.1029/2022JA030903>

Martinis, C., J. Meriwether, M. Biondi, R. Niciewjewski, C. Fesen, and M. Mendillo (2001), Zonal neutral winds at equatorial and low-latitudes, *J. Atmos. Sol. Terr. Phys.*, 63, 1559–1569.

Martinis, C., Eccles, J. V., Baumgardner, J., Manzano, J., & Mendillo, M. (2003). Latitude dependence of zonal plasma drifts obtained from dual-site airglow observations. *Journal of Geophysical Research*, 108(A3), 1129. <https://doi.org/10.1029/2002JA009462>

Mendillo, M., and Baumgardner, J. (1982), Airglow characteristics of equatorial plasma depletions, *J. Geophys. Res.*, 87(A9), 7641– 7652, doi:10.1029/JA087iA09p07641.

Mendillo, M., and Tyler, A. (1983), Geometry of depleted plasma regions in the equatorial ionosphere, *J. Geophys. Res.*, 88(A7), 5778– 5782, doi:10.1029/JA088iA07p05778.

McClintock, W. E., Eastes, R. W., Beland, S., Bryant, K. B., Burns, A. G., Correira, J., et al (2020). Global-scale Measurements of the Limb and Disk (GOLD) Mission Implementation: 2. Observations, Data Pipeline and Level 1 Data Products. *Journal of Geophysical Research: Space Physics*, 125, e2020JA027809. <https://doi.org/10.1029/2020JA027809>.

Pallamraju, D., Karan, D. K., and Phadke, K. A. (2016), First three dimensional wave characteristics in the daytime upper atmosphere derived from ground-based multiwavelength oxygen dayglow emission measurements, *Geophys. Res. Lett.*, 43, 5545– 5553, doi:10.1002/2016GL069074.

Raghavarao, R., L. E. Wharton, N. W. Spencer, H. G. Mayr, and L. H. Brace (1991), An equatorial temperature and wind anomaly (ETWA), *Geophys. Res. Lett.*, 18 (7), 1193–1196, doi:10.1029/91GL01561.

Richmond, A. D. (1995), Ionospheric electrodynamics using magnetic apex coordinates, *J. Geomagn. Geoelectr.*, 47, 191–212, <https://doi.org/10.5636/jgg.47.191>.

Rishbeth, H (1972), Thermospheric winds and the F-region: A review, *Journal of Atmospheric and Terrestrial Physics*, 34, [https://doi.org/10.1016/0021-9169\(72\)90003-7](https://doi.org/10.1016/0021-9169(72)90003-7).

Sultan, P. J. (1996), Linear theory and modeling of the Rayleigh-Taylor instability leading to the occurrence of equatorial spread F, *J. Geophys. Res.*, 101(A12), 26875– 26891, doi:10.1029/96JA00682.

Taori, A., A. K. Patra, and L. M. Joshi (2011), Gravity wave seeding of equatorial plasma bubbles: An investigation with simultaneous F region, E region, and middle atmospheric measurements, *J. Geophys. Res.*, 116, A05310, doi:10.1029/2010JA016229.

Thébault, E., Finlay, C.C., Beggan, C.D. et al. (2015), International Geomagnetic Reference Field: the 12th generation. *Earth Planet Sp* 67, 79, doi:10.1186/s40623-015-0228-9.

Tsunoda, R. T., R. C. Livingston, and C. L. Rino (1981), Evidence of a velocity shear in bulk plasma motion associated with the post-sunset rise of the equatorial F layer, *Geophys. Res. Lett.*, 8, 807–810, doi:10.1029/GL008i007p00807.

Valladares, C. E., J. W. Meriwether, R. Sheehan, and M. A. Biondi, Correlative study of neutral winds and scintillation drifts measured near the magnetic equator, *J. Geophys. Res.*, 107(A7), 1112, doi:10.1029/2001JA000042, 2002.

Woodman, R. F., and C. La Hoz (1976), Radar observations of F region equatorial irregularities, *J. Geophys. Res.*, 81, 5447.

Yoshimura, R., N. Iwagami, and K.-I. Oyama (2003), Rocket measurement of electron density and atomic oxygen density modulated by atmospheric gravity waves, *Adv. Space Res.*, 32, 837–842.

426

427 Zalesak, S.T., Ossakow, S.L., Chaturvedi, P.K., (1982), Nonlinear equatorial spread F: The effect
428 of neutral winds and background Pedersen conductivity. J. Geophys. Res 87, 151.

429 <https://doi.org/10.1029/93ja00762>.